# Development of a micro-mechanical model for the determination of damage properties of cement pastes

Abderrahmane Rhardane, Frederic Grondin, Syed Yasir Alam

# Development of a micro-mechanical model for the determination of damage properties of cement pastes

Abderrahmane Rhardane, Frédéric Grondin*, Syed Yasir Alam

Institut de Recherche en Génie Civil et Mécanique (GeM), UMR 6183, Centrale Nantes – Université de Nantes - CNRS 1 rue de la Noë, 44321 Nantes, France

* Corresponding author: frederic.grondin@ec-nantes.fr

## Abstract

Demand on low-carbon concrete for building increases in many countries. However, workers in construction sites are often confronted with early cracking risks in concrete when new cement mixtures are used. Indeed, new chemical additions are mixed with cement and mixtures are optimized in laboratories to reach the target performance for concrete. But, in site, the results are not exactly the same. In order to help concrete suppliers design new low-carbon concrete, it is necessary to control the cracking risk of concrete. To consider all phenomena into concrete, a modelling approach starting at the micro-scale seems to be the best tool for the prediction of any concrete mixture in any environment. A numerical protocol at the micro-scale is proposed in order to determine the damage properties of cement pastes. The method is based on a once-for-all calibration of parameters which remain unchanged for any other mixtures. Validations were made using tensile and compressive tests on different cement pastes. The numerical results are in good agreement with experimental data of four cement pastes with different water-to-cement ratios and mineral additions, and of six mixtures obtained from the literature. The results demonstrate the predictive power of the numerical approach and its utility for a quick assessment of material properties.

## Keywords

Cement pastes; Micro-mechanics; Damage; Finite element model

# 1 Introduction

This study aims to give a decision-making tool to concrete suppliers to design new low-carbon concretes. Many customers ask for high performance concrete structures with low cement content by replacing it with mineral additions (fly ash, slag, etc.) [1–3]. But, workers in construction sites observe more cracking in new concretes than in classical concretes. The links between cracking in these new concretes with environmental conditions and casting methods are not totally clear. Concrete suppliers assess the strength of concrete in laboratories, albeit under controlled conditions. In addition to that, only statistical evaluations can be done by linking the influence of one component on the global behaviour. New concrete mixtures need to define the properties of the new cement paste by performing numerous tests.

In order to limit the tests, many researchers have given elastic properties of the concrete components to link the global behaviour to the mixture. These properties, obtained by nano-indention measurements, were also used in models and gave good results in comparison with elastic tests. However, under inelastic loading, these models used empirical parameters for fracture properties [4–8]. So, for new concrete mixtures, new adjustments are necessary. It is thus unpractical to use the previous approach to understand the influence of environmental conditions and casting methods under non-controlled conditions, as in construction sites.

On another note, in order to correctly predict the durability of low-carbon concrete structures, multi-physics models need to use physical properties reflecting real processes. It seems therefore important to consider damage properties not dependant on the mixture and test conditions to predict damage of a variety of cementitious materials [9–11].

It is very difficult to consider all the details of the cement paste's microstructure in a unique volume for modelling without undermining the computation time. Indeed, two scales can be considered: a molecular scale ($10^{-8}$ to $10^{-6}$ m) [12–15] and a microscopic scale ($10^{-6}$ to $10^{-4}$ m). The first is used to calculate the intrinsic properties of the components independently of the hydration or loading. The second considers an assembly of the last components, obtained by cement hydration, with properties that are linked to the properties obtained by the first method, or found via experimental measurements.

In this respect, a representative elementary volume (REV) is defined to represent the cement paste. The REV should be small enough to consider all the components in an explicit manner, and big enough to represent a macroscopic sample of the heterogeneous material. A size of 100 µm is often used by authors [16–21]. Others, however, suggest smaller [22,23] or bigger sizes [17,24], in the range of 50 µm to 400 µm. The choice of the REV is made according to

the size of the biggest inclusion, usually five times the diameter of the largest inclusion [25]. The simulations start with the generation of a virtual microstructure of the cement paste whose phase assemblage mimics the real distribution and composition of phases in the real microstructure. This can be achieved by means of numerical hydration models. Several codes and tools have been developed for this, and a review of the available hydration models can be found in Thomas et al. [26].

In the present study, the Virtual Cement and Concrete Testing Laboratory (VCCTL) platform [24] has been chosen for the cement paste's microstructure generation. This programme, which is based on the cellular architecture of CEMHYD3D [27,28], allows for an explicit representation of the cement phases as well as the incorporation of admixtures such as slag, fly ash and silica fume. Consequently, a mesh algorithm [29] was used to import the hydrated cement paste volume in the finite element code Cast3M [30] for mechanical simulations.

In this paper, a micro-mechanical approach for the determination of the damage properties of cement pastes is proposed. The objective of this approach is to avoid the multiple tests for the characterization and readjustment of the mechanical properties. The elastic properties of the cement paste's components were founded in the literature. The damage model of Fichant et al. [31] was chosen for its simplicity and quality to simulate the mechanical damage of cement-based materials. This damage model is independent of the scale and correctly reproduces the softening behaviour of a damaged material. A parametric study was performed with the goal to find the relationship between the damage properties of the cement paste's components.

First of all, the numerical method is described in three sections: the cement type chosen and the virtual representation obtained from VCCTL are presented, the damage model used in the finite element modelling is given in detail, and the numerical protocol is explained to show the unknown parameters to identify. Second of all, the numerical results regarding the damage properties of the cement paste's components are discussed. Finally, simulations for tensile and compressive tests are compared to experimental data for a wide range of cement types.

# 2 Presentation of the micro-mechanical approach

## 2.1 Tested materials and virtual cement hydration

A typical Portland cement paste contains about a dozen cement phases. This includes unhydrated particles with clinker phases and sulfates (gypsum, hemihydrate and anhydrite), and the products of hydration which mainly contain calcium silicate hydrate (or C-S-H), portlandite, ettringite and sulfo-aluminates (AFm). The number of phases in composite

cements increases sharply in the presence and the hydration of slags, fly ash, silica fume, fillers and other minor phases. The gradual formation of hydrates and their distribution within the matrix provide the cement paste with increasing cohesion, stiffness and strength.

The mineral compositions of the cements incorporated in the VCCTL model are listed in Table 1. The composition of Portland cements, labelled CEM-N1 and -N2, were obtained from their technical files while the data for the remaining cements are extracted from the "CemBase" database compiled by the Nanocem consortium [32,33]. These cement paste compositions that are considered in micro-mechanical simulations are divided into three sets:

- The first set consists of only one cement paste, labelled CP1-0.45, used as a reference point for the identification of failure properties of cement paste phases. This cement paste is made from ordinary Portland cement (CEM-N1) with a water-to-binder ratio of 0.45.
- The second set consists of three cement pastes used for the testing of the model on other compositions. Two of these cement pastes are made from CEM-N1 with w/b= 0.4 and 0.5 (labelled CP1-0.4 and CP1-0.5, respectively), while the third is made from CEM-N2 with w/b=0.45 (labelled CP2-0.45).
- Using data available from the literature, the third set consists of 23 cement pastes, used by the model to predict their respective compressive strengths. 18 of these are composed of other Portland cements (labelled CEM-IA, -IB…-IF) while the remaining five are made of composite cements with different admixtures (cf. Table 1).

It should be noted that cement phases are explicitly represented inside the microstructure volume, including C-S-H and capillary porosity. The term "phase" is used here in the same sense used in the hydration model VCCTL. Therefore, the C-S-H gel, which can be decomposed into low density C-S-H, high density C-S-H and gel porosity [31], is considered as a single phase and is represented by one voxel type. Water-filled porosity is also counted as another "phase", regardless of the water content in the capillary voids. A full list of the phases included in the VCCTL model is available on the programme's online user guide.

The representativeness of the REV of the cement paste is controlled by the resolution of the microstructure voxels ($1\mu m^3$, as imposed by the hydration model) and its size. Taking into account the grading curve of the cement (99% of particles are smaller than 60µm in size), a $200\times200\times200\mu m^3$ cube was chosen as REV. The simulation of hydration in VCCTL proceeds by cycles. A conversion of cycles into units of time would not be necessary if the user is only interested in the evolution of the degree of hydration (which is the case for the third set of cement pastes). However, selecting the hydrating microstructure at the exact age of 28 days is needed to determine the micro-mechanical parameters from experimental results.

**Table 1.** ***Mineral composition of cements used and mix compositions of cement pastes (Values represent mass fractions. Clinker phase fractions are given on a clinker basis).***

| Cement Phases / Cement pastes | | Primary constituents of cement | | | | | | | Secondary constituents | | | | | |
|---|---|---|---|---|---|---|---|---|---|---|---|---|---|---|
| | | Clinker phases | | | | | | Sulfates | Calcium carbonate | Limestone | Slag | Silica fume | Quartz | Fly ash |
| **Label** | **w/b (DoH %)** ‡ | $C_3S$ | $C_2S$ | $C_3A$* | $C_4AF$ | $K\bar{S}$ | $N\bar{S}$ | $C\bar{S}H_x$ † | | | | | | |
| **CEM-N1** | **0.4 (67.3 %)** **0.45 (69.7 %)** **0.5 (76.9 %)** | 72.2 | 9.4 | 9.4 | 7.3 | 1.3 | 0.3 | 4.2 | 1 | 1 | 0 | 0 | 0 | 0 |
| **CEM-N2** | **0.45 (65.3 %)** | 69.1 | 9.1 | 7.5 | 11.4 | 2.8 | 0.2 | 1.5 | 6 | 2 | 0 | 0 | 0 | 0 |
| **CEM-IA** | **0.677 (90.2 %)** **0.497 (84.9 %)** **0.32 (61.4 %)** | 66.9 | 8.0 | 14.1 | 4.4 | 0 | 0 | *4.6*** | 0 | 0 | 0 | 0 | 0 | 0 |
| **CEM-IB** | **0.688 (87.4%)** **0.505 (82.3 %)** **0.325 (60.3 %)** | 67.5 | 7.0 | 6.0 | 10.0 | 0 | 0 | *4.6*** | 0 | 0 | 0 | 0 | 0 | 0 |
| **CEM-IC** | **0.681 (83.6 %)** **0.503 (79.6 %)** **0.323 (60 %)** | 58.0 | 18.2 | 8.0 | 10.0 | 0 | 0 | *3.2*** | 0 | 0 | 0 | 0 | 0 | 0 |
| **CEM-ID** | **0.454 (73.8 %)** **0.364 (64.7 %)** **0.274 (55.1 %)** | 63.2 | 13.3 | 2.0 | 12.9 | 0 | 0 | *4.3*** | 0 | 0 | 0 | 0 | 0 | 0 |
| **CEM-IE** | **0.683 (82.3 %)** **0.502 (77 %)** **0.323 (47.2 %)** | 54.5 | 19.2 | 8.4 | 9.8 | 0 | 0 | *3.1*** | 0 | 0 | 0 | 0 | 0 | 0 |
| **CEM-IF** | **0.681 (84.7 %)** **0.501 (78.7 %)** **0.323 (59.1 %)** | 55.5 | 18.2 | 8.4 | 9.8 | 0 | 0 | *3.1*** | 0 | 0 | 0 | 0 | 0 | 0 |
| **CEM-H0** | **0.51 (82.4 %)** | 60.7 | 22.1 | 6.3 | 10.9 | 0 | 0 | 3.6 | 0 | 0 | 0 | 0 | 0 | 0 |
| **CEM-HQ** | **0.55 (91.3 %)** | 60.7 | 22.1 | 6.3 | 10.9 | 0 | 0 | 3.6 | 0 | 0 | 0 | 0 | 45 | 0 |
| **CEM-HS** | **0.53 (86.3 %)** | 60.7 | 22.1 | 6.3 | 10.9 | 0 | 0 | 3.6 | 0 | 0 | 45 | 0 | 0 | 0 |
| **CEM-HF** | **0.60 (85.6 %)** | 60.7 | 22.1 | 6.3 | 10.9 | 0 | 0 | 3.6 | 0 | 0 | 0 | 0 | 0 | 45 |
| **CEM-HL** | **0.54 (85.6 %)** | 60.7 | 22.1 | 6.3 | 10.9 | 0 | 0 | 3.6 | 0 | 45 | 0 | 0 | 0 | 0 |

* *Contains both orthorhombic and cubic forms of $C_3A$.*

** *Data unavailable. The estimated values are derived from cements with similar composition.*

† *Includes all phases of added sulfates (gypsum or dihydrate, hemihydrate and anhydrite).*

‡ *w/b = water-to-binder ratio. doH = degree of hydration.*

In order to relate each cycle with the correct hydration time and extract the microstructure at 28 days, isothermal calorimetry is conducted using the same cement paste compositions of the first and second sets. In this experimental setup, the heat released by the hydration reactions is recorded as a function of time, and then correlated to the heat release calculated by VCCTL, as suggested by the hydration model's manual (Figure 1).

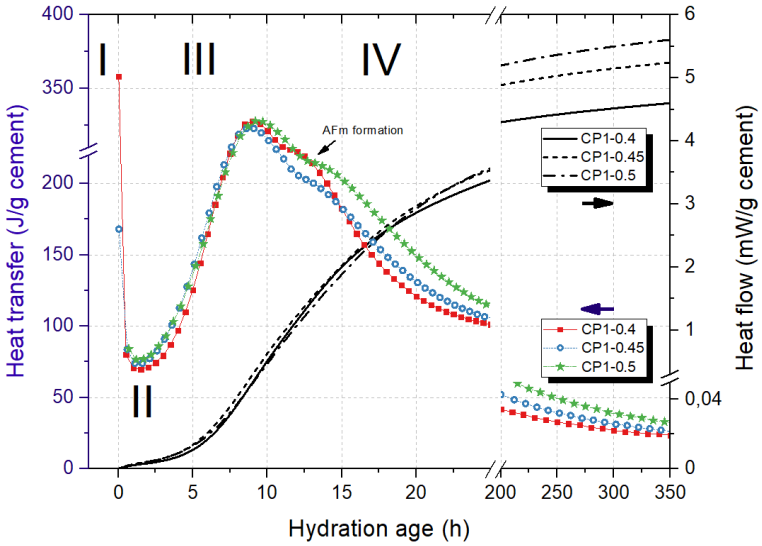


**Figure 1.** ***Heat release during hydration of virtual cement pastes (from 0h to 24h, with a step of 5 hours, then up to 14 days).***

The virtual microstructure generated by VCCTL is shown in Figure 2. Since 3D simulations were practically impossible due to the high number of voxels, 2D sections were extracted and the simulations were conducted in 2D plane stress by considering a thin thickness. This assumption is pertinent, because small displacements are considered, and, at each numerical step, they are smaller than the thickness, far from the edge. The macroscopic results were averaged over four sections (labelled S50, S100, S150 and S200, as illustrated in Figure 3). In the finite element model, the different colours (or grey level) represent each cement paste's components: *purple*=porosity, *red*=$C_3S$, *orange*=$C_2S$, *blue*=$C_3A$, *light blue*=$C_4AF$, *dark blue*=sulfates, *white*=inert particles, *yellow*=CH, *pink*=C-S-H, *green*=hydrogarnet and AFm, *light green*=ettringite (cf. 2D sections in Figure 3).

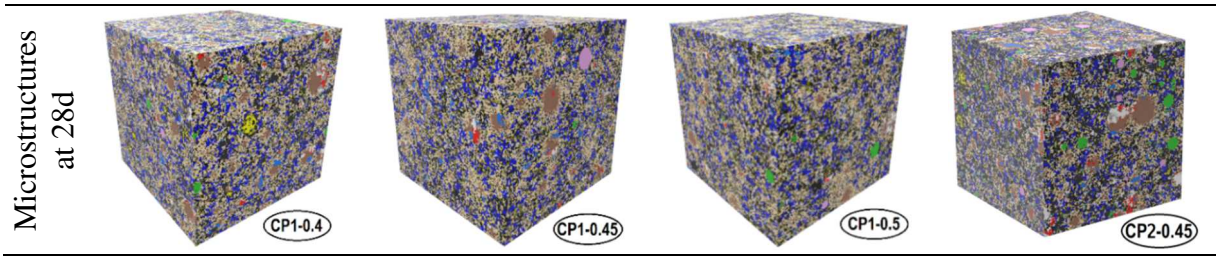


**Figure 2.** ***3D virtual cement pastes obtained by VCCTL.***

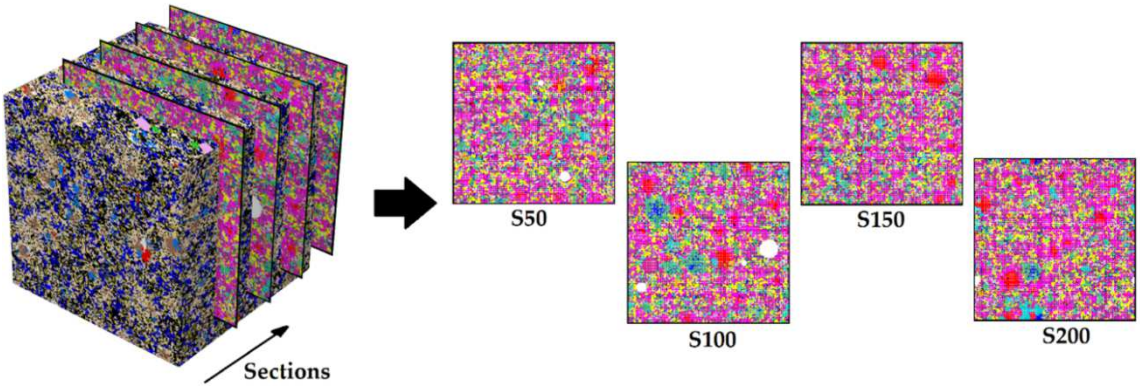


**Figure 3.** ***Extraction of sections S50, S100, S150 and S200 from the 3D microstructure.***

## 2.2 Damage model

### 2.2.1 Problem formulation

Several models have been proposed for the simulation of damage in cementitious materials. The model chosen to represent the local damage of cement phases inside the microstructure is Fichant's model [31,35] based on the microplane model proposed in [36] and the damage law of Mazars [37]. For the sake of simplicity, the isotropic description of the model is used. According to the principles of damage theory, the effective stress tensor $\tilde{\sigma}$ and the total stress σ of the material can be expressed in terms of the elastic strain tensor such as:

$$\begin{aligned} \tilde{\boldsymbol{\sigma}} &= \mathbb{C}^{\boldsymbol{d}}\, \boldsymbol{\epsilon}^{\boldsymbol{e}} \\ \boldsymbol{\sigma} &= \mathbb{C}^{\mathbf{0}}\, \boldsymbol{\epsilon}^{\boldsymbol{e}} \end{aligned} \tag{1}$$

where $\mathbb{C}^{d}$ and $\mathbb{C}^{0}$ denote the fourth-order stiffness tensors for damaged and undamaged states, respectively. The relationship between the two tensors is given by [35]:

$$\mathbb{C}^{\boldsymbol{d}} = (\mathbb{I} - \mathbb{D})\mathbb{C}^{\mathbf{0}} \tag{2}$$

where $\mathbb{D}$ is the damage tensor, which can be simplified to $\mathbb{D} = D\mathbb{I}$ in the isotropic case of the model. In the absence of plasticity, the evolution of damage is controlled by the following loading surface $f$:

$$f(\bar{n}) = \bar{n}\boldsymbol{\epsilon}^{\boldsymbol{e}}\bar{n} - \kappa_0 \tag{3}$$

To ensure that damage of cement phases grows only due to tension, only the tensile (positive) components of the eigenstrain tensor are taken into account [37]. In this case, the equivalent strain $\epsilon_{EQ}$ is used:

$$\bar{n}\boldsymbol{\epsilon}^{\boldsymbol{e}}\bar{n} = \epsilon_{EQ} = \sqrt{\langle\epsilon_{11}\rangle_+^2 + \langle\epsilon_{22}\rangle_+^2 + \langle\epsilon_{33}\rangle_+^2} \tag{4}$$

where $\epsilon_{ii}$ represents the eigenvalues of the strain tensor and $\langle\cdot\rangle_+$ are the Macaulay brackets. The evolution of the damage law due to tensile microcracking in the isotropic model takes the following exponential form [38]:

$$\begin{cases} f = 0 \; and \; \dot{\epsilon}_{EQ} > 0 \rightarrow \dot{D} = \dfrac{\kappa_0(1 + B_T\epsilon_{EQ})}{\epsilon_{EQ}^2}\exp\left[-B_T\left(\epsilon_{EQ} - \kappa_0\right)\right] \\ f < 0 \; or \; \dot{\epsilon}_{EQ} = 0 \rightarrow \dot{D} = 0 \end{cases} \quad (5)$$

with $\kappa_0$ denoting the strain damage threshold and $B_T$ the strain softening slope parameter which is linked to mode I fracture energy. These model parameters can be calculated from the measurable mechanical properties of cement phases using the equations [38,39]:

$$\kappa_0 = \frac{f_t}{E} \qquad B_T = \frac{f_t}{\dfrac{G_f}{h} - \dfrac{f_t\kappa_0}{2}} \quad (6)$$

where E, $f_t$ and $G_f$ represent respectively the Young's modulus, tensile strength and fracture energy of the cement phase. The above expression of $B_T$ ensures that the energy dissipated in a finite element during damage is independent of the mesh by introducing the characteristic size h [38].

For the sake of simplicity, the same isotropic damage model was applied to all cement phases. However, the mechanical parameters, namely E, ν, $f_t$ and $G_f$, differ from phase to phase (see section 2.2.2). Damage in the cement paste is initiated by the local build-up of stress and would progress through the weakest links in the material. It is assumed that the four mechanical properties are not dependant on the cement paste mixture type and the test conditions for each phase. It is rather the matrix's content and the phase assemblage that affect the macroscopic behaviour of the cement paste.

### 2.2.2 Elastic properties of the cement paste's phases

Many researchers have measured elastic properties of the cement paste's components (see references in the summary table 2). In this study, and for each elastic parameter, it is the average of all the values found in the literature that is used in the simulations (Table 2). It should be noted that these properties do not include the capillary porosity, which is modelled as a separate "phase". The capillary porosity was given small values for the elastic properties which were calibrated using experimental measurements of Young's modulus in cement paste CP1-0.45 (following the suggested values in [40,41]). Elastic properties of C-S-H are homogenized, assuming that C-S-H at the micro-scale is a mixture of 70% low density C-S-H and 30% high density C-S-H [42].

202 **Table 2.** ***Elastic properties of the cement paste phases.***

| Cement phases | | | E (GPa) | $\nu$ (-) | Ref. |
|---|---|---|---|---|---|
| **Clinker phases** | Alite | $C_3S$ | 137.4 | 0.299 | [17,24,43–45] |
| | Belite | $C_2S$ | 135.5 | 0.297 | [17,24,43–47] |
| | Celite | $C_3A$ | 145.2 | 0.278 | [17,24,43–47] |
| | Ferrite | $C_4AF$ | 150.8 | 0.318 | [17,24,43–46,48] |
| | Arcanite | $K\bar{S}$ | 44.2 | 0.269 | [17,49] |
| | Thenardite | $N\bar{S}$ | 57.1 | 0.281 | [17,48] |
| **Gypsum** | Gypsum | $C\bar{S}H_2$ | 44.5 | 0.33 | [17,24,43,46,50] |
| | Bassanite | $C\bar{S}H_{0.5}$ | 132.0 | 0.25 | [17,24,48] |
| | Anhydrite | $C\bar{S}$ | 88.8 | 0.233 | [17,24,51] |
| **Admixtures** | Slags | $\S$ | 137.4 | 0.299 | [17,24,43–45] |
| | Silica fume | $\S$ | 71.7 | 0.169 | Same as $SiO_2$ |
| | AS glass | $C_xS_yA_z$ | 71.7 | 0.169 | Same as $SiO_2$ |
| | Inert | $\S$ | 71.0 | 0.296 | [21] |
| **Main hydrates** | Portlandite | $CH$ | 43.5 | 0.294 | [17,24,32,43,52–54] |
| | C-S-H | $C_{1.7}SH_4$ | 23.8 | 0.24 | [42,55] |
| | Hydro-garnet | $C_3AH_6$ | 93.8 | 0.32 | [14,17] |
| | Ettringite | $C_6A\bar{S}_3H_{32}$ | 24.1 | 0.321 | [14,17,24,32,43] |
| | Monosulfate | $C_4A\bar{S}H_{12}$ | 43.2 | 0.292 | [14,17,24,32] |
| | Iron hydroxide | $FH_3$ | 22.4 | 0.25 | [17] |
| | Calcite | $C\bar{C}$ | 97.0 | 0.296 | [56] |
| | Limestone | $C$ | 183.9 | 0.21 | [48] |
| **Secondary hydrates** | Iron-rich ettringite | $C_6(A.F)\bar{S}_3H_{32}$ | 24.1 | 0.321 | Same as ettringite |
| | Pozzolanic / slag C-S-H | $\S$ | 23.8 | 0.24 | Same as C-S-H |
| | Friedel's salt | $C_3A(CaCl_2)H_{10}$ | 22.4 | 0.25 | [17] |
| | Strätlingite | $C_2ASH_8$ | 22.4 | 0.25 | [17,57] |
| | Calcium mono-carbonate | $C_4A\bar{C}H_{11}$ | 79.0 | 0.25 | [17,58] |
| | Brucite | $MH$ | 83.3 | 0.183 | [57] |
| | Magnesium sulphate | $M\bar{S}$ | 10.5 | 0.1 | [59] |
| **Pores** | Porosity (wet) | $H$ | 1.9 | 0.499 | - |
| | Porosity (dry) | Ø | 1.9 | 0.001 | - |

## 2.3 Numerical protocol for the determination of the damage properties of phases

The damage properties of the cement phases depend on their nature, morphology and porosity. For crystalline phases which exist naturally, or in the case of hydrates which can be synthetized, some mechanical properties have already been evaluated and can be founded in the literature (see [11,53,60] for a few examples). For other phases with a more complex nature such as C-S-H, nano-indentation or molecular dynamics simulations can be used. A review of the recent techniques that can be used to determine such properties is given in Zhang et al. [61].

It is important not to confound properties measured on pure materials with those of the porous phases in cement paste, as porosity considerably affects their mechanical properties. For instance, the Young's modulus of compacted ettringite powder is equal to 52 GPa while that of ettringite formed in cement paste is in the order of 25 GPa [17]. Since it is difficult to take into account all the heterogeneities of the cement paste, and due to the lack of damage properties of many phases, some assumptions are put forward for a numerical determination of these properties:

1. Each voxel in the finite element mesh corresponds to a unique homogenous phase,
2. All voxels of the same type have the same mechanical properties,
3. The behaviour of the phases is isotropic,
4. All phases obey the damage model presented above,
5. The tensile strength is proportional to the micro-hardness (or HD), according to a constant coefficient $\alpha_{ft}$, such as: $HD = \alpha_{ft} \times f_t$,
6. The fracture energy of each phase is proportional to the elastic energy, according to a constant coefficient $\beta_{Gf}$, as follows: $G_f = \beta_{Gf} \frac{(1+\nu) f_t^2}{E}$.

Assumptions 1 and 3 decrease the number of elastic properties to two parameters: E and $\nu$. Assumptions 5 and 6 render it possible to write the relationship between unknown failure properties ($f_t$ and $G_f$) with other known properties which can be easily measured by nano-indention (E, $\nu$ and HD). For ductile materials, the empirical relation between hardness and strength is given by: $HD = 3f_t$ [62]. For composites, granular materials, brittle glasses and ceramics, the proportionality coefficient is found between 28 and 200 [62].

The parameters $\alpha_{ft}$ and $\beta_{Gf}$ are assumed to be constants. This strong hypothesis is made considering that it is practically impossible to identify all the damage properties of the cement

phases. It is for this reason that the damage parameters found for the cement phases should be considered as "intrinsic" to the damage model being used here. However, unlike older studies [5,18] where the values given for the two parameters $\alpha_{ft}$ and $\beta_{Gf}$ are arbitrary, the parameters are fixed using an inverse analysis scheme. They are determined using the following strategy:

1. First, the mix design for the reference cement paste CP1-0.45 is prepared for experimental testing. Since cement paste is generally too brittle to effectively conduct direct tensile tests, CMOD-controlled three-point bending tests were conducted in sealed conditions to avoid drying-induced microcracking, as illustrated in Figure 4. The crack formation is monitored via the displacement called CMOD, or Crack Mouth Opening Displacement, which consists of the measurement of the lateral displacement of the notch at the bottom of the beam, representing the initial crack. The notch is carefully made by inserting a thin bar (~0.8mm) in the mould before casting the cement paste, as shown in Figure 4. Moreover, compressive strength was determined on 4x4x4cm cubic volumes of the same cement paste.

**Figure 4.** ***Prepared cement paste beams for the CMOD-controlled three-point bending test.***

2. The unknown macroscopic properties of cement paste such as the tensile strength and the fracture energy were determined from the force-CMOD response obtained in the previous step using the methodology described in [63,64]. The obtained values for $f_{t,paste}$ and $G_{f,paste}$ can then be used to determine $\alpha_{ft}$ and $\beta_{ft}$ in the following steps.
3. At the microscopic level, the virtual microstructure of CP1-0.45 is generated using VCCTL, as described above, and the REV is converted into a finite element mesh in the FE code Cast3M. The damage model is then applied to all phases, with the elastic properties given in Table 2 attributed to each corresponding phase. Initial values were given to $\alpha_{ft}$ and $\beta_{Gf}$ as a starting point for inverse identification. Isostatic boundary conditions have been applied with imposed displacement $u_{imp}$ varying within the interval [0; 10µm]. The discretization of this interval is given in Figure 5. Indeed, the

displacement increment is not constant because the first steps require more precision for computational convergence. This discretization is thus chosen as a compromise between precision, convergence and speed. The final value of 10µm is satisfactory enough to obtain the total stress-crack opening curve, which allows for the calculation of the numerical fracture energy from the softening slope.

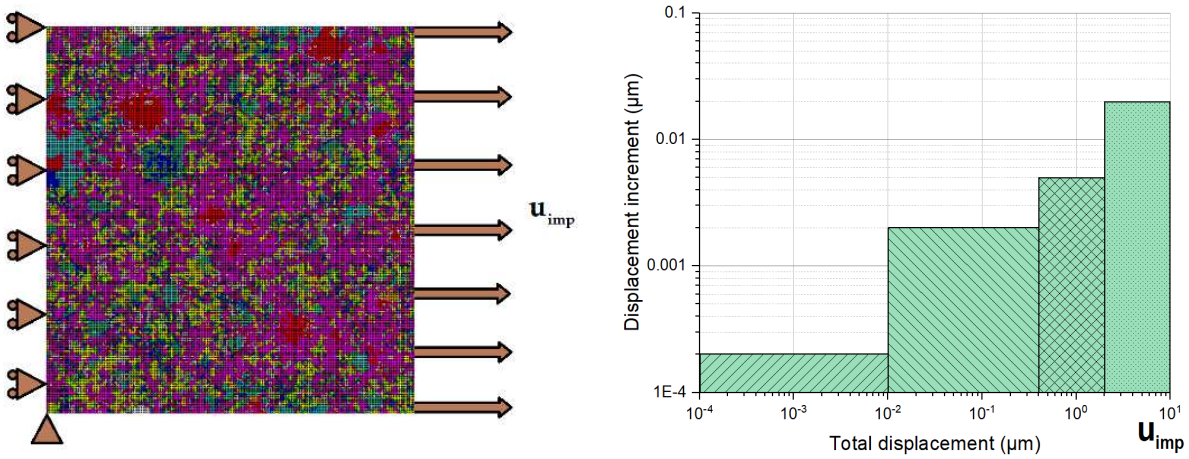


**Figure 5.** ***Numerical simulation of the tensile test: imposed boundary conditions (left) and imposed displacement increments (right).***

4. The unknown parameters cannot be easily determined using optimization tools such as the Levenberg-Marquardt method [65]. This is because both $\alpha_{ft}$ and $\beta_{Gf}$ influence the macroscopic damage properties, $f_t$ and $G_f$, in an unknown manner, and the solution might not be unique. Therefore, an alternative is proposed, in the form of a design of experiments (DOE). In this parametric study, numerical "experiments" are conducted by simulating tensile and compressive tests on cement paste microstructures, which can be used to determine their macroscopic properties. The influence of the parameters $\alpha_{ft}$ and $\beta_{Gf}$ can be established, and this allows for a quick determination of $\alpha_{ft}$ and $\beta_{Gf}$ without the need for the complicated algorithms of inverse analysis. This step is explained in more detail in 3.1.
5. Once $\alpha_{ft}$ and $\beta_{Gf}$ are determined, the effective damage parameters of cement phases are assumed to be independent of the cement paste mixture and test conditions, and can be used in the damage model proposed above for other compositions. Only the volume fractions and the distributions of the cement paste's phases inside the virtual microstructure affect the global properties of the representative cement paste volume.

# 3 Results and discussion

## 3.1 Calculation of the damage properties of the cement paste's phases

Initial calculations showed that the adjustment of $\alpha_{ft}$ and $\beta_{Gf}$ affects simultaneously the tensile strength and the fracture energy of the cement paste CP1-0.45 at the macroscopic scale. If the micro-mechanical properties are to be determined, it must be proven that the inverse problem converges to a unique solution. This means that for a certain cement paste with given macroscopic properties, there is a unique couple $(\alpha_{ft}, \beta_{Gf})$ which gives these properties.

Let $\mathcal{F}: \mathbb{R}^2 \to \mathbb{R}^2$ be defined as the function linking each couple of the micro-mechanical parameters $(\alpha_{ft}, \beta_{Gf})$ to the macroscopic properties $(f_t, G_f)$ of the cement paste. Tensile tests of the cement paste FC1-0.45 were simulated by varying $\alpha_{ft}$ and $\beta_{Gf}$ within the restricted domain $[15;\ 35] \times [1.25 \times 10^{-5};\ 6.25 \times 10^{-5}] \in \mathbb{R}^2$. This domain is selected as it gives realistic values for $f_t$ and $G_f$. The macroscopic properties, determined for each fixed value of $(\alpha_{ft}, \beta_{Gf})$, are mapped in Figure 6 as a function of two parameters. The results show that $\mathcal{F}$ is subjective over the restricted domain of interest.

Therefore, the existence of the unique solution to the previous problem requires that $\mathcal{F}$ be injective. In other words, the isocontours of $f_t(\alpha_{ft}, \beta_{Gf})$ and $G_f(\alpha_{ft}, \beta_{Gf})$ projected on the $(\alpha_{ft}, \beta_{Gf})$ plane must always intersect at a unique point. The isocontours are lines that represent a constant value of the function $\mathcal{F}$.

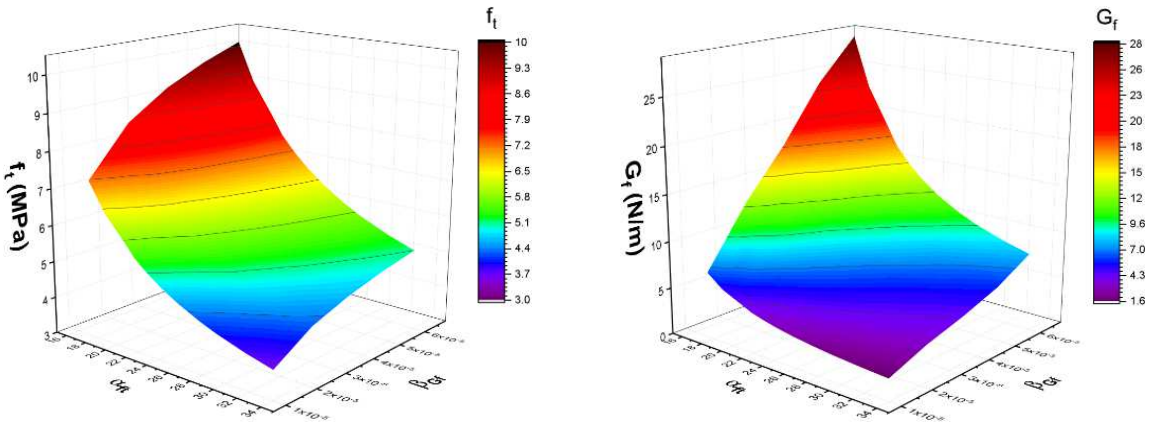


**Figure 6.** ***Influence of $\alpha_{ft}$ and $\beta_{Gf}$ on the tensile strength (left) and on the failure energy (right).***

The projected isocontours of $f_t$ and $G_f$, plotted in Figure 7, show that both $\alpha_{ft}$ and $\beta_{Gf}$ affect the strength and fracture energy of cement paste, with $f_t$ strongly influenced by $\alpha_{ft}$ and slightly increasing with $\beta_{Gf}$ for low $\alpha_{ft}$. On the other hand, $G_f$ is influenced equally by $\alpha_{ft}$ and $\beta_{Gf}$, but barely changes with respect to $\alpha_{ft}$ when $\beta_{Gf}$ is low.

This is expected, since any increase in the tensile strength of individual cement phases contributes to the total strength of the cement paste, while the increase of the fracture energy of phases with low tensile strength opposes the rapid development of damage and therefore slightly contributes to the overall strength. On the other hand, a low value for $\beta_{Gf}$ means that cement paste's phases are very brittle, and the increase of their tensile strength will not contribute to the overall fracture energy. It can deduced from the pattern of the isocontours that, for any given value of $(f_t, G_f)$, there is a unique point of intersection in the restricted domain. This method makes it possible to directly determine the couple $(\alpha_{ft}, \beta_{Gf})$ which coincides with the experimental values of $f_t = 6.7$ MPa and $G_f = 6.6 J/m^2$ corresponding to the reference cement paste CP1-0.45. The point of intersection, drawn in Figure 8, matches the determined values: $\alpha_{ft} = 20.2$ and $\beta_{Gf} = 3.75 \times 10^{-5}$. This allows for calculating the damage properties of cement paste's phases, which are summarized in Table 3.

The obtained value for $\alpha_{ft}$ suggests that the behaviour of cement paste's phases is, on average, more brittle than ductile metals ($\alpha_{ft} = 3$), but remains less brittle than most ceramics ($28 < \alpha_{ft} < 183$) [62]. The calculated tensile strength of C-S-H is equal to 55 MPa, which is lower than values of 264-700 MPa [53] or 66-107 MPa [32] found by other authors. On the other hand, the obtained fracture energy for C-S-H falls in the expected range of 4.4-20 J/m² [11,53]. This difference in the order of magnitude can be partially explained by the fact that the experimental values determined in [53] were flexural strengths measured on micro-beams which are not purely homogeneous, or due to the underlying assumptions made by the authors [32] regarding the hydrates.

The assumptions taken here for the identification of the damage properties of cement paste's phases also affect the values found for the model parameters. It should therefore be understood that the properties found in this study are contingent on the damage model used for the behaviour of cement paste's phases. Nevertheless, these properties of cement paste's phase are not dependent on the composition of the microstructure.

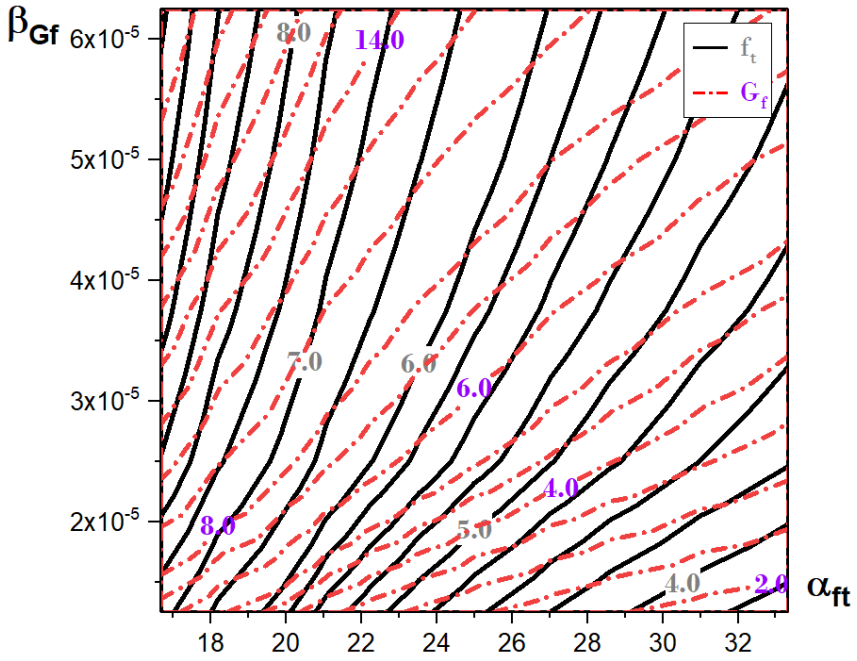


**Figure 7. Iso***contours of the functions $f_t$ (black solid lines) and $G_f$ (red dashed lines) projected on the $(\alpha_{ft}, \beta_{Gf})$ plane. It is clear that: 1) the solid lines never cross each other, and the same goes for the dashed lines, and 2) every red dashed line crosses any black solid line once and only once. The two observations mean that, for any fixed values of $f_t$ and $G_f$, the corresponding isocontours cross at a unique point, which gives the unique values for $(\alpha_{ft}, \beta_{Gf})$.*

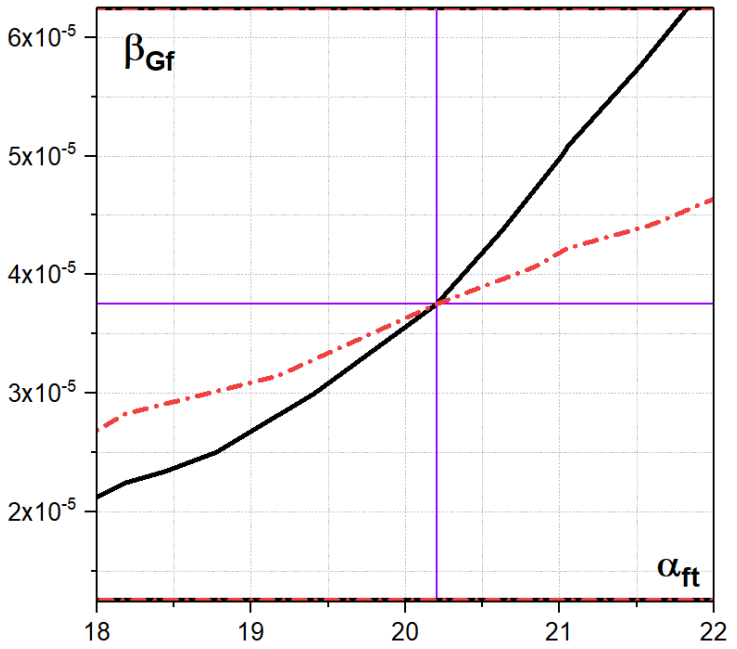


**Figure 8.** *Determination of the unique couple $(\alpha_{ft}, \beta_{Gf})$ from the isocontours corresponding to the experimental values of $(f_t, G_f)$.*

354 **Table 3.** ***Micro-mechanical damage properties of the main cement paste phases.***

| Cement phases | | | $f_t$ (MPa) | $G_f$ (J/m²) |
|---|---|---|---|---|
| **Clinker phases** | Alite | $C_3S$ | 430.7 | 65.8 |
| | Belite | $C_2S$ | 396.0 | 56.3 |
| | Celite | $C_3A$ | 534.6 | 94.3 |
| | Ferrite | $C_4AF$ | 470.3 | 72.5 |
| | Arcanite | $K\bar{S}$ | 29.7 | 1.0 |
| | Thenardite | $N\bar{S}$ | 62.9 | 3.3 |
| **Gypsum** | Gypsum | $C\bar{S}H_2$ | 29.6 | 1.0 |
| | Bassanite | $C\bar{S}H_{0.5}$ | 61.7 | 1.4 |
| | Anhydrite | $C\bar{S}$ | 93.6 | 4.6 |
| **Admixtures** | Slags | § | 430.7 | 65.8 |
| | Silica fume | § | 346.5 | 73.4 |
| | AS glass | $C_xS_yA_z$ | 346.5 | 73.4 |
| | Inert | § | 69.3 | 3.3 |
| **Main hydrates** | Portlandite | $CH$ | 73.8 | 6.1 |
| | C-S-H | $C_{1.7}SH_4$ | 55.0 | 5.9 |
| | Hydro-garnet | $C_3AH_6$ | 324.7 | 55.6 |
| | Ettringite | $C_6A\bar{S}_3H_{32}$ | 39.6 | 3.2 |
| | Monosulfate | $C_4A\bar{S}H_{12}$ | 262.4 | 77.3 |
| | Iron hydroxide | $FH_3$ | 292.1 | 178.5 |
| | Calcite | $C\bar{C}$ | 69.3 | 2.4 |
| | Limestone | $C$ | 111.2 | 3.1 |
| **Secondary hydrates** | Iron-rich ettringite | $C_6(A.F)\bar{S}_3H_{32}$ | 39.6 | 3.2 |
| | Pozzolanic / slag C-S-H | § | 55.0 | 5.9 |
| | Friedel's salt | $C_3A(CaCl_2)H_{10}$ | 76.2 | 12.2 |
| | Strätlingite | $C_2ASH_8$ | 328.2 | 225.4 |
| | Calcium mono-carbonate | $C_4A\bar{C}H_{11}$ | 262.3 | 40.9 |
| | Brucite | $MH$ | 49.5 | 1.3 |
| | Magnesium sulphate | $M\bar{S}$ | 41.6 | 6.8 |
| **Pores** | Porosity (wet) | $H$ | 0.001*<br>0.017** | ~0*<br>0.02** |
| | Porosity (dry) | Ø | 0.001 | ~0 |

* Calibrated for tension ** Calibrated for compression

355

## 3.2 Validation by a tensile failure test

The macroscopic response along the direction $i$ is calculated from the macroscopic stress $\Sigma_i$ and the strain $E_i$. However, in order to determine the macroscopic fracture energy, the post-peak displacement due to crack opening, $\Delta U_i^{pp}$, is deduced from the computed displacement field, as suggested in [39], and the macroscopic fracture energy is calculated as the area below the $\Sigma_i - \Delta U_i^{pp}$ curve.

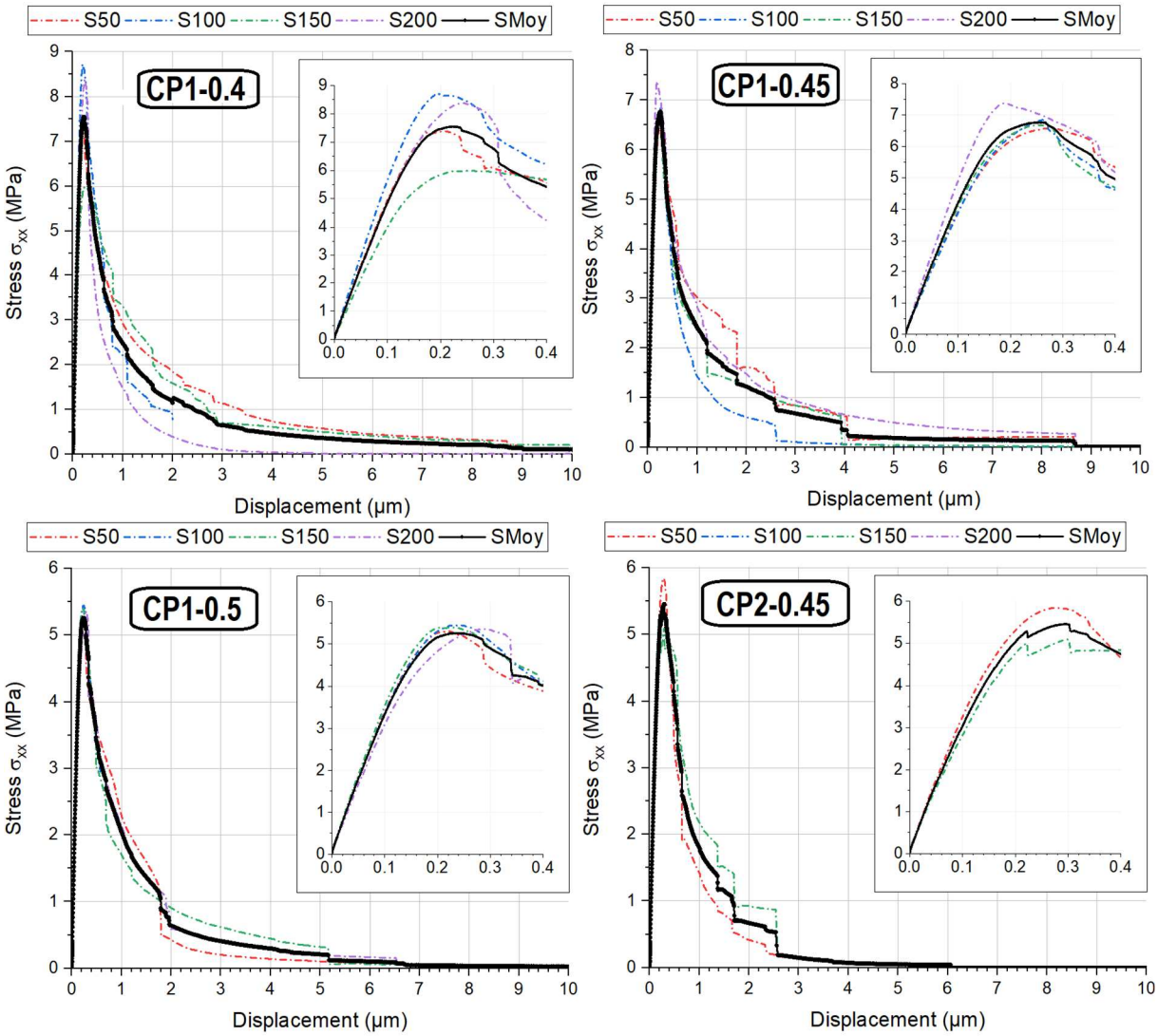


**Figure 9.** ***Macroscopic responses ($\Sigma_X - \Delta U_X$) in tension for different cement paste compositions.***

Figures 9 show the global stress-displacement response for CP1-0.45, as well as for the second set of cement pastes FC1-0.4, CP1-0.5 and CP2-0.45, respectively. The inset graphs represent the first stage of the response around the maximal stress values. The difference

between the behaviours along the two load directions $X$ and $Y$ amounts to less than 5%. For this reason, only the responses along the $X$ direction are shown.

The Young's modulus, the tensile strength and the fracture energy were calculated for the four cement pastes and compared to experimentally-measured values, as shown in Figure 10.

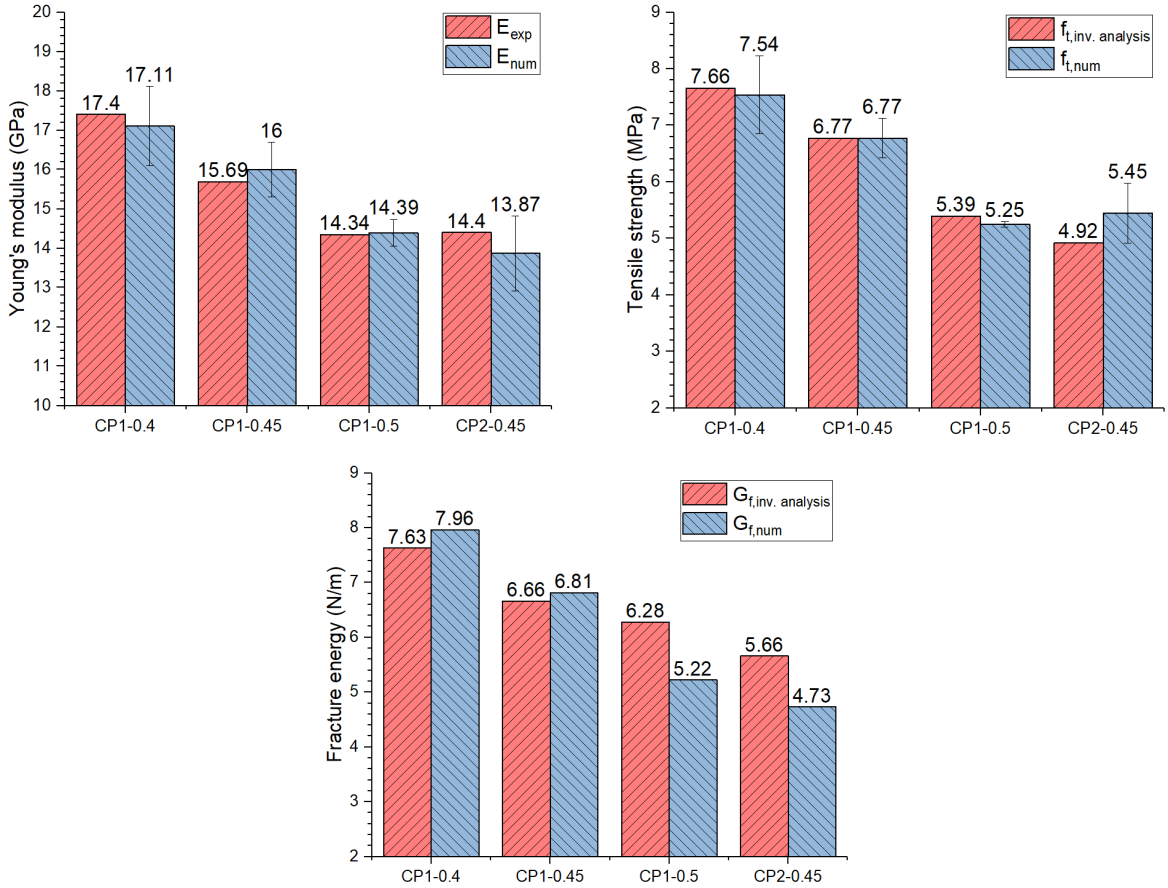


**Figure 10.** ***Comparison between numerical calculations and experimental measurements for E, $f_t$ and $G_f$.***

Error bars for the simulation results correspond to the differences between each simulated sections of the cement paste volume. The Young's modulus $E$ was determined from the initial slope of the curve $\Sigma_X - E_X$ in the pre-peak region, and no difference was found between the two loading directions. The tensile strength $f_t$ was identified as the maximal stress reached, and $G_f$ corresponds to the area under the $\Sigma_X - \Delta U_X^{pp}$ curve.

Comparisons show that numerical results are in fairly good agreement with the experimental values, even for the cement paste CP2 with a different cement containing calcite. This result corroborates the proper selection of the REV and the model parameters for the phases. In addition to that, the results show that the calibration made using only one cement paste to

386 determine the properties of the model is sufficient to simulate different cement paste
387 compositions without the need for a new calibration of model parameters.
388

## 389 3.3 Validation by a compressive test

390 Using the above calculated parameters, compressive tests are simulated for all cement
391 pastes and the results are compared to the experimental data. For the second set of cement
392 pastes, the experimental compressive strength was determined using a classical compression
393 test on $4\times4\times4cm$ cubes. For the third set, cement paste microstructures were generated using
394 VCCTL, based on the data available in the CemBase database [66]. Since the isothermal
395 calorimetry curves of the cements were not given, hydration is simulated until the targeted
396 degree of hydration which corresponds to the age at which the compression test is conducted
397 by the authors of the CemBase, as shown in Table 1. The macroscopic stress-displacement
398 curves of CP1-0.4, CP1-0.45, CP1-0.5 and CP2-0.45 are plotted in Figure 11: black lines
399 (labelled SMoy) represent the average curve of the results obtained from the four sections,
400 and the shaded areas represent the standard deviation.
401 Calculations in compression were performed for more cement pastes containing mineral
402 additions in place of cement. The numerical estimations for the compressive strength of all
403 cement pastes are drawn against experimental values in Figure 12. This figure shows the
404 relevance of the model to numerically estimate the compressive strength of low-carbon
405 cement pastes. The shaded area corresponds to a margin of ±2 MPa and the error bars
406 represent the standard deviation.
407 Unlike in tension, the damage of cement paste in compression is not stable. For cement pastes
408 made with CEM-N1, the applied stress drops sharply after reaching its peak value. For CP2-
409 0.45 made from type II cement (CEM-N2), the stress maintains a steady state before total
410 failure. This can be attributed to the presence of large pores left after the dissolution of
411 calcium carbonate in CP2-0.45, which is mostly reactive due to its high amount in CEM-N2
412 [67]. The presence of large pores acts as arrest mechanisms to the development of
413 microcracks.

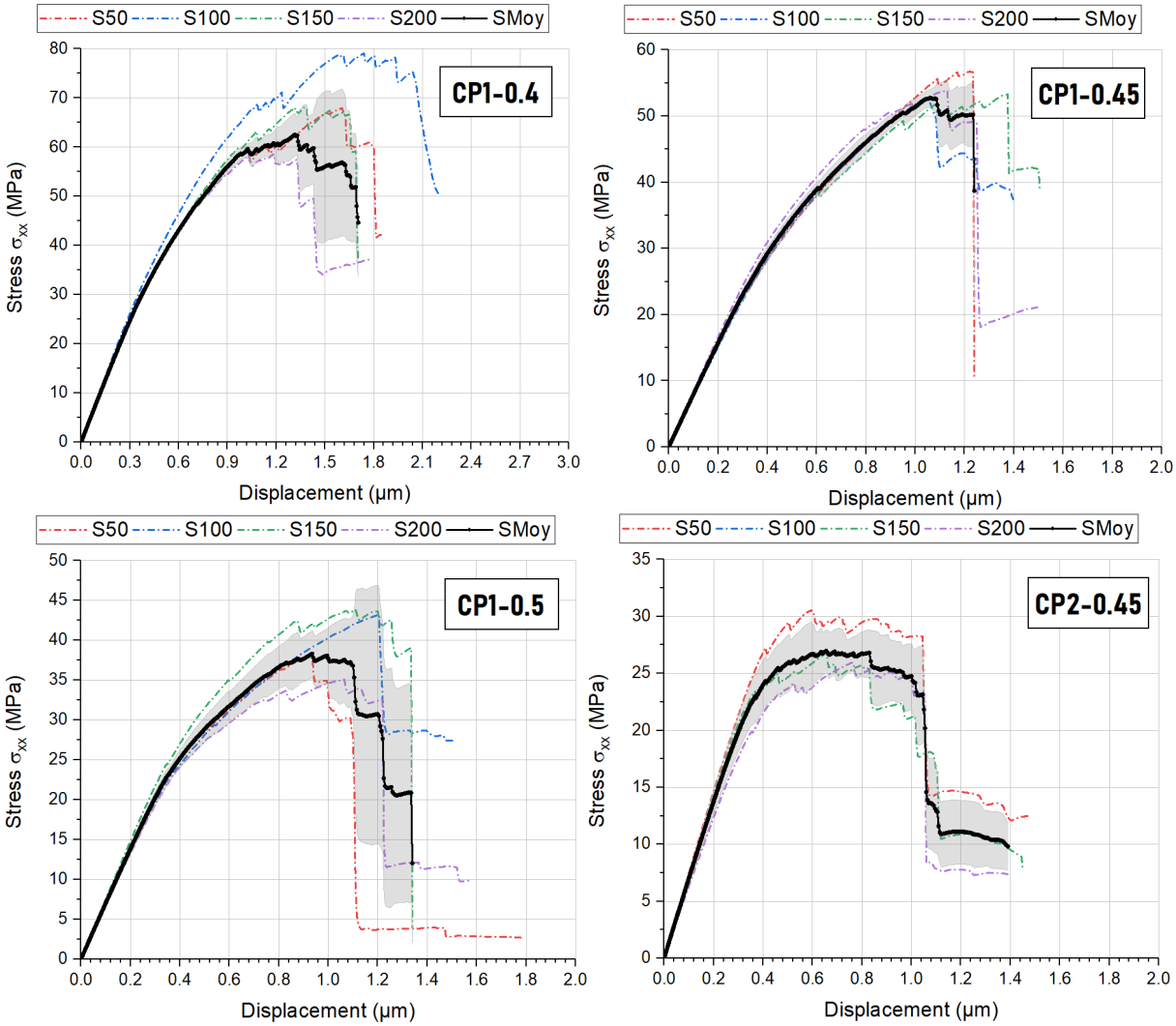


414
415 **Figure 11.** ***Macroscopic responses in compression for different cement paste compositions.***
416

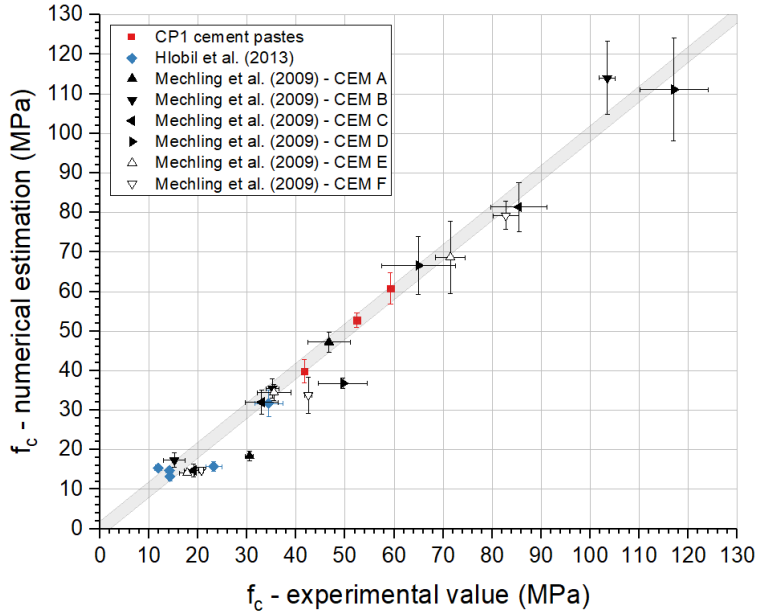


417
418 **Figure 12.** ***Compressive strengths of cement pastes: numerical-experimental comparison.***

As observed, the numerical value of the compressive strength for CP1 cement pastes matches the experimental results within a margin of ±2 MPa (the experimental value for CP2-0.45 was not retrieved). For the third set of cement pastes, the lower the w/b ratio, the bigger the standard deviation between the numerical results of the same cement paste composition. This is also observed experimentally, and can be explained by the low porosity in compositions with low w/b ratios. For these compositions, the cement is only partially hydrated, and large particles of unhydrated clinker remain in the matrix. Therefore, these particles force the crack profile to change course between sections.

For the most part, the experimental results are predicted by the model to a satisfactory degree. In some cases, the modelling approach underestimates the compressive strength. This can be partially attributed to the lack of complete data regarding the cements from the CemBase database, such as the grading curve and the energy activation of cements, which were only assumed based on similar cements from the database of the hydration model. Nevertheless, the proposed model is able to provide quick estimations of the strength of cement pastes without adjusting any of its parameters.

## 3.4 Use of the model for the analysis of the local damage at the micro-scale

One important aspect of this micro-mechanical modelling approach is its ability to track the local behaviour which can be difficult to do during experimental testing. Using the model, it is possible to follow microscopic observations of mechanical shields during the test, the correlation between the cracking pattern and specific phases of the cement paste, the initiation and propagation of microcracks as well as the measurement of the crack openings, etc.

Figure 13 shows the damage maps extracted from CP1-0.45 at different steps of loading: at 60% pre-peak, at the peak, and at 20% post-peak, with the crack opening profile at 20% post-peak calculated according to [39], and Scanning Electron Microscopic (SEM) observations of the crack pattern in cement pastes obtained from [68]. To clarify the illustration of cement phases, all anhydrous particles in the damage maps are shown in white, hydrates in grey and porosity in black.

It can be deduced that no significant damage occurs when 60% of the load is applied in the pre-peak region (only 18 finite elements are damaged). At the peak load, microcracks begin to coalesce and form short branches that develop mainly at the interface between anhydrous phases and hydrates, as shown in Figure 13-3 (numerical) and 13-6 (experimental). These branches remain for the most part unconnected, which provides cement paste with a softening

curve that is characteristic of a semi-stable fracture behaviour [8,69]. When the applied load reaches 20% in the post-peak region, microcracks merge to form major macrocracks that propagate along the weakest links and perpendicular to the loading direction. This is clearly observed in the crack opening profile in Figure 13-4.

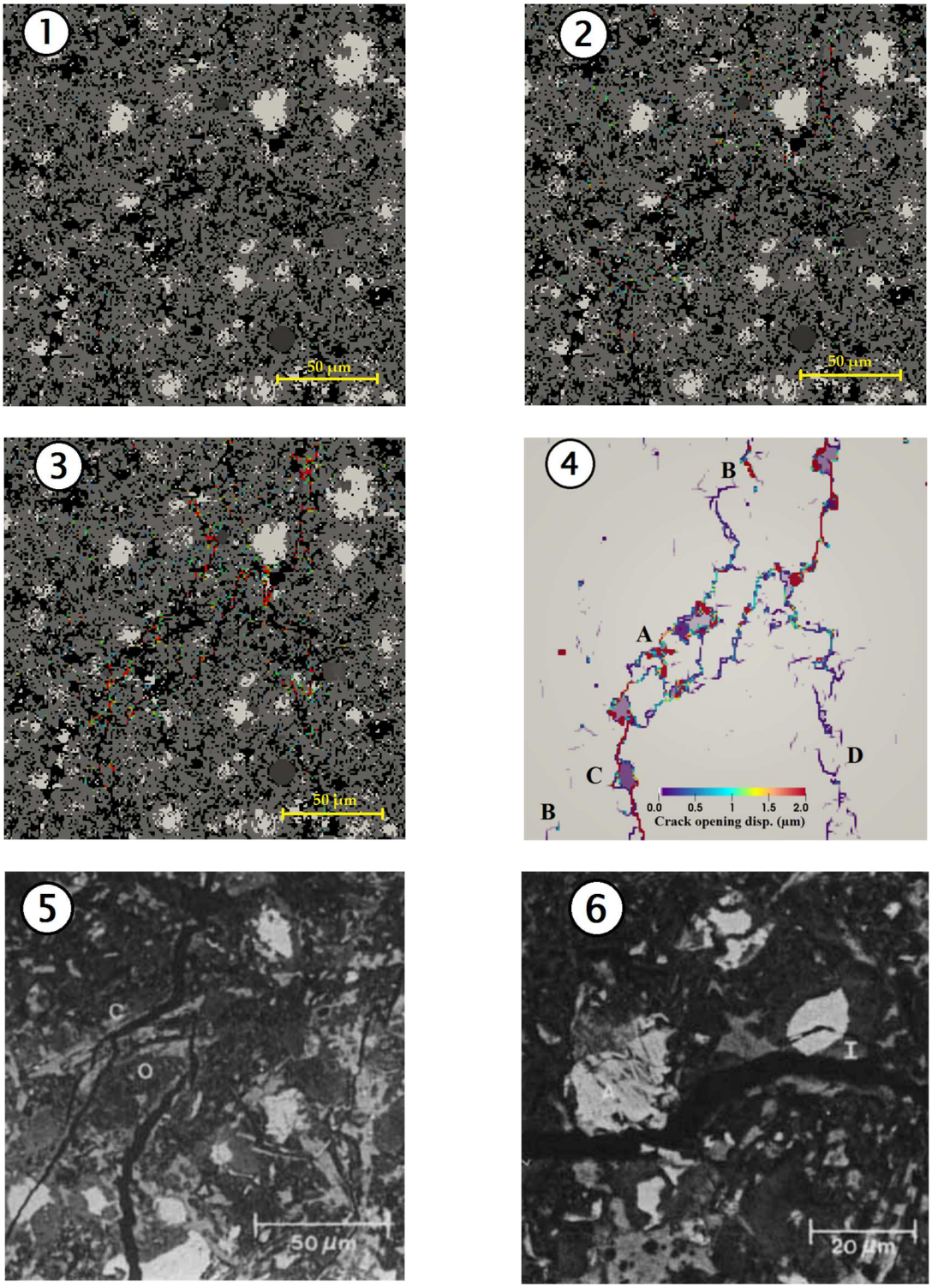


**Figure 13.** ***Damage maps at 60% pre-peak (1), at the peak (2) and at 20% post-peak (3). Crack opening profile at 20% post-peak (4). Crack pattern obtained by SEM observations (5 and 6).***

When a crack reaches anhydrous particles, deviation and branching (A) occur due to the high resistance of clinker grains. This crack bifurcation is also observed in SEM images (cf. Figure 12-5). In some cases, cracks can be arrested (B) or present offset (C) due to the presence of large portlandite crystals which remain undamaged. Microstructural features of crack also include the presence of a zigzag pattern (D) comprised of short segments ~10µm in length, which is attested by SEM observations by other authors [68].

# 4 Conclusions and perspectives

The presented study aims to contribute to the development of a numerical method for the determination of the damage properties of cement pastes for general use. In other words, the objective of this study is to provide a tool for rapid assessment of properties of different cement pastes, and therefore a tool that can be used for the optimization and the development of low-carbon concretes in order to decrease the climate impact of concrete industry.

For this reason, a micro-mechanical modelling approach is developed to identify the damage properties of all cement paste phases, including the mineral additions which are used in low-carbon cements. The method proposed to calculate these properties identifies values for the model parameters that are independent of the cement paste mixture and test conditions, and therefore can be used for any cement paste without calibration. Based on experimental data from nano-indention tests found in the literature, the approach suggests calibrating only two parameters, which were remain constant for all cement paste compositions. This approach can be used in a similar way for other damage models, according to the number of unknown parameters. Simulations of both tensile and compressive tests are conducted on cement pastes with various mix designs, including low-carbon cement pastes, and then compared to the measured experimental values. The results demonstrate the utility of the modelling approach to estimate the properties of cement pastes, including strengths and fracture energy, without resorting to experimental tests or repetitive fitting of model parameters.

Because the model gives the global mechanical response of the cement paste, it is then possible to extract the homogenized properties and use them at the upper scale (i.e. mortar and concrete scales). This provides a calibration-free method to quickly assess the main properties of different concrete in order to optimize their mix designs. The approach also allows for a close investigation of microcracking patterns and crack profiles. First tests were conducted at the mortar scale for an ordinary cement to simulate the failure of mortar beams [70]. On

another note, coupling the mechanical damage with thermal, hydraulic or chemical processes and phenomena is possible, starting at the microscale. This allows for a better evaluation of the damage patterns that involve complex multi-physics simulations. Evaluations of the sort, such as freeze-thaw cycles, high temperatures, creep and shrinkage, have been performed and analysed in order to validate the models, and will be published following the basics of the proposed approach. A decision-making tool for concrete suppliers can therefore be utilized for optimization and evaluation of material properties and behaviours.

# 5 References


[1] P.J.M. Monteiro, S.A. Miller, A. Horvath, Towards sustainable concrete, Nat. Mater. 16 (2017) 698–699. doi:10.1038/nmat4930.

[2] B. Ozorhon, Response of Construction Clients to Low-Carbon Building Regulations, J. Constr. Eng. Manag. 139 (2013) A5013001. doi:10.1061/(asce)co.1943-7862.0000768.

[3] Q.D. Nguyen, M.S.H. Khan, A. Castel, T. Kim, Durability and Microstructure Properties of Low-Carbon Concrete Incorporating Ferronickel Slag Sand and Fly Ash, J. Mater. Civ. Eng. 31 (2019) 04019152. doi:10.1061/(ASCE)MT.1943-5533.0002797.

[4] F. Bernard, S. Kamali-Bernard, W. Prince, 3D multi-scale modelling of mechanical behaviour of sound and leached mortar, Cem. Concr. Res. 38 (2008) 449–458. doi:10.1016/J.CEMCONRES.2007.11.015.

[5] Z. Qian, E. Schlangen, G. Ye, K. Van Breugel, Prediction of mechanical properties of cement paste at microscale, Mater. Construcción. 60 (2010) 7–18. doi:10.3989/mc.2010.55209.

[6] Z. Qian, Multiscale Modeling of Fracture Processes in Cementitious Materials, 2012.

[7] M. Zhang, C.N. Morrison, A.P. Jivkov, A Lattice-spring Model for Damage Evolution in Cement Paste, Procedia Mater. Sci. 3 (2014) 1854–1859. doi:10.1016/j.mspro.2014.06.299.

[8] M. Luković, E. Schlangen, G. Ye, Combined experimental and numerical study of fracture behaviour of cement paste at the microlevel, Cem. Concr. Res. 73 (2015) 123–135. doi:10.1016/j.cemconres.2015.03.008.

[9] M.R. Hardisty, R. Zauel, S.M. Stover, D.P. Fyhrie, The Importance of Intrinsic Damage Properties to Bone Fragility: A Finite Element Study, J. Biomech. Eng. 135 (2012) 011004. doi:10.1115/1.4023090.

[10] H.S. Witsenhausen, The Intrinsic Model for Discrete Stochastic Control: Some Open Problems, in: Control Theory, Numer. Methods Comput. Syst. Model., Springer, Murray Hill, New Jersey, 1975: pp. 322–335. doi:10.1007/978-3-642-46317-4_24.

[11] B. Šavija, H. Zhang, E. Schlangen, Micromechanical testing and modelling of blast furnace slag cement pastes, Constr. Build. Mater. 239 (2020) 117841. doi:10.1016/j.conbuildmat.2019.117841.

[12] R.J.-M. Pellenq, A. Kushima, R. Shahsavari, K.J. Van Vliet, M.J. Buehler, S. Yip, F.-J. Ulm, A realistic molecular model of cement hydrates., Proc. Natl. Acad. Sci. U. S. A. 106 (2009) 16102–16107. doi:10.1073/pnas.0902180106.

[13] D. Hou, Y. Zhu, Y. Lu, Z. Li, Mechanical properties of calcium silicate hydrate (C–S–H) at nano-scale: A molecular dynamics study, Mater. Chem. Phys. 146 (2014) 503–511. doi:10.1016/J.MATCHEMPHYS.2014.04.001.

[14] S. Hajilar, B. Shafei, Mechanical failure mechanisms of hydrated products of tricalcium aluminate: A reactive molecular dynamics study, Mater. Des. 90 (2016) 165–176. doi:10.1016/j.matdes.2015.10.089.

[15] G. Geng, R.J. Myers, J. Li, R. Maboudian, C. Carraro, D.A. Shapiro, P.J.M. Monteiro, Aluminum-induced dreierketten chain cross-links increase the mechanical properties of nanocrystalline calcium aluminosilicate hydrate, Sci. Rep. 7 (2017) 44032. doi:10.1038/srep44032.

[16] G. Ye, Z. Sun, T. Voigt, K. van Breugel, S.P. Shah, A micromechanic model for characterization of cement paste at early age validated with experiments, Int. RILEM Symp. Concr. Sci. Eng. A Tribut. to Arnon Bentur. (2004) 1–11.

[17] C.-J. Haecker, E.J. Garboczi, J.W. Bullard, R.B. Bohn, Z. Sun, S.P. Shah, T. Voigt, Modeling the linear elastic properties of Portland cement paste, Cem. Concr. Res. 35 (2005) 1948–1960. doi:10.1016/j.cemconres.2005.05.001.

[18] F. Bernard, S. Kamali-Bernard, Performance simulation and quantitative analysis of cement-based materials subjected to leaching, Comput. Mater. Sci. 50 (2010) 218–226. doi:10.1016/j.commatsci.2010.08.002.

[19] L. Liu, G. Ye, E. Schlangen, H. Chen, Z. Qian, W. Sun, K. van Breugel, Modeling of the internal damage of saturated cement paste due to ice crystallization pressure during freezing, Cem. Concr. Compos. 33 (2011) 562–571. doi:10.1016/J.CEMCONCOMP.2011.03.001.

[20] H. Zhang, B. Šavija, S. Chaves Figueiredo, M. Lukovic, E. Schlangen, Microscale Testing and Modelling of Cement Paste as Basis for Multi-Scale Modelling., Mater.

(Basel, Switzerland). 9 (2016). doi:10.3390/ma9110907.

[21] X. Ouyang, G. Ye, K. van Breugel, Experimental and numerical evaluation of mechanical properties of interface between filler and hydration products, Constr. Build. Mater. 135 (2017) 538–549. doi:10.1016/j.conbuildmat.2017.01.022.

[22] V. Šmilauer, Z. Bittnar, Microstructure-based micromechanical prediction of elastic properties in hydrating cement paste, Cem. Concr. Res. 36 (2006) 1708–1718. doi:10.1016/j.cemconres.2006.05.014.

[23] H. Zhang, B. Šavija, S.C. Figueiredo, E. Schlangen, Experimentally validated multi-scale modelling scheme of deformation and fracture of cement paste, Cem. Concr. Res. 102 (2017) 175–186. doi:10.1016/J.CEMCONRES.2017.09.011.

[24] L. Valentini, M. Parisatto, V. Russo, G. Ferrari, J.W. Bullard, R.J. Angel, M.C. Dalconi, G. Artioli, Simulation of the hydration kinetics and elastic moduli of cement mortars by microstructural modelling, Cem. Concr. Compos. 52 (2014) 54–63. doi:10.1016/j.cemconcomp.2014.05.005.

[25] A.A. Gusev, Representative volume element size for elastic composites: A numerical study, J. Mech. Phys. Solids. 45 (1997) 1449–1459. doi:10.1016/S0022-5096(97)00016-1.

[26] J.J. Thomas, J.J. Biernacki, J.W. Bullard, S. Bishnoi, J.S. Dolado, G.W. Scherer, A. Luttge, Modeling and simulation of cement hydration kinetics and microstructure development, Cem. Concr. Res. 41 (2011) 1257–1278. doi:10.1016/j.cemconres.2010.10.004.

[27] D.P. Bentz, Three-Dimensional Computer Simulation of Portland Cement Hydration and Microstructure Development, J. Am. Ceram. Soc. 80 (1997) 3–21. doi:10.1111/j.1151-2916.1997.tb02785.x.

[28] D.P. Bentz, CEMHYD3D: A Three-Dimensional Cement Hydration and Microstructure Development Modelling Package. Version 2.0, NIST Interagency/Internal Rep. - 6485. (2000). https://www.nist.gov/publications/cemhyd3d-three-dimensional-cement-hydration-and-microstructure-development-modelling-0 (accessed August 6, 2018).

[29] B. Hilloulin, D. Hilloulin, F. Grondin, A. Loukili, N. De Belie, Mechanical regains due to self-healing in cementitious materials: Experimental measurements and micro-mechanical model, Cem. Concr. Res. 80 (2016) 21–32. doi:10.1016/J.CEMCONRES.2015.11.005.

[30] P. Verpaux, T. Charras, A. Millard, CASTEM 2000 une approche moderne du calcul des structures, Calc. Des Struct. Intell. Artif. Plur. (1988) 261–271. http://www-

592 cast3m.cea.fr.
593 [31] S. Fichant, G. Pijaudier-Cabot, C. La Borderie, Continuum damage modelling:
594 Approximation of crack induced anisotropy, Mech. Res. Commun. 24 (1997) 109–114.
595 doi:10.1016/S0093-6413(97)00001-3.
596 [32] M. Hlobil, V. Šmilauer, G. Chanvillard, Micromechanical multiscale fracture model for
597 compressive strength of blended cement pastes, Cem. Concr. Res. 83 (2016) 188–202.
598 doi:10.1016/j.cemconres.2015.12.003.
599 [33] J.-M. Mechling, A. Lecomte, C. Diliberto, Relation between cement composition and
600 compressive strength of pure pastes, Cem. Concr. Compos. 31 (2009) 255–262.
601 doi:10.1016/J.CEMCONCOMP.2009.02.009.
602 [34] P.C. Fonseca, H.M. Jennings, J.E. Andrade, A nanoscale numerical model of calcium
603 silicate hydrate, Mech. Mater. 43 (2011) 408–419. doi:10.1016/j.mechmat.2011.05.004.
604 [35] S. Fichant, C. La Borderie, G. Pijaudier-Cabot, Isotropic and anisotropic descriptions of
605 damage in concrete structures, Mech. Cohesive-Frictional Mater. 4 (1999) 339–359.
606 doi:10.1002/(SICI)1099-1484(199907)4:4<339::AID-CFM65>3.0.CO;2-J.
607 [36] Z.P. Bažant, J. Ožbolt, Nonlocal Microplane Model for Fracture, Damage, and Size
608 Effect in Structures, J. Eng. Mech. 116 (1990) 2485–2505. doi:10.1061/(ASCE)0733-
609 9399(1990)116:11(2485).
610 [37] J. Mazars, Application de la mécanique de l'endommagement au comportement non
611 linéaire et à la rupture du béton de structure, 1984.
612 https://trid.trb.org/view.aspx?id=1032710 (accessed July 23, 2018).
613 [38] M. Matallah, M. Farah, F. Grondin, A. Loukili, E. Rozière, Size-independent fracture
614 energy of concrete at very early ages by inverse analysis, Eng. Fract. Mech. 109 (2013)
615 1–16. doi:10.1016/j.engfracmech.2013.05.016.
616 [39] M. Matallah, C. La Borderie, O. Maurel, A practical method to estimate crack openings
617 in concrete structures, Int. J. Numer. Anal. Methods Geomech. 34 (2009) 1615–1633.
618 doi:10.1002/nag.
619 [40] M.M. Shahzamanian, T. Tadepalli, a. M. Rajendran, W.D. Hodo, R. Mohan, R.
620 Valisetty, P.W. Chung, J.J. Ramsey, Representative Volume Element Based Modeling
621 of Cementitious Materials, J. Eng. Mater. Technol. 136 (2013) 011007.
622 doi:10.1115/1.4025916.
623 [41] V. Šmilauer, Z.P. Bažant, Identification of viscoelastic C-S-H behavior in mature
624 cement paste by FFT-based homogenization method, Cem. Concr. Res. 40 (2010) 197–
625 207. doi:10.1016/J.CEMCONRES.2009.10.003.

626 [42] G. Constantinides, F.J. Ulm, The effect of two types of C-S-H on the elasticity of
627 cement-based materials: Results from nanoindentation and micromechanical modeling,
628 Cem. Concr. Res. 34 (2004) 67–80. doi:10.1016/S0008-8846(03)00230-8.
629 [43] J.S. Dolado, K. van Breugel, Recent advances in modeling for cementitious materials,
630 Cem. Concr. Res. 41 (2011) 711–726. doi:10.1016/j.cemconres.2011.03.014.
631 [44] P. Mondal, Nanomechanical Properties of Cementitious Materials, Northwestern
632 University, 2008. https://www.numis.northwestern.edu/thesis/Thesis-Paramita.pdf
633 (accessed July 26, 2018).
634 [45] K. Velez, S. Maximilien, D. Damidot, G. Fantozzi, F. Sorrentino, Determination by
635 nanoindentation of elastic modulus and hardness of pure constituents of Portland
636 cement clinker, Cem. Concr. Res. 31 (2001) 555–561. doi:10.1016/S0008-
637 8846(00)00505-6.
638 [46] P. Termkhajornkit, Q.H. Vu, R. Barbarulo, S. Daronnat, G. Chanvillard, Dependence of
639 compressive strength on phase assemblage in cement pastes: Beyond gel–space ratio —
640 Experimental evidence and micromechanical modeling, Cem. Concr. Res. 56 (2014) 1–
641 11. doi:10.1016/j.cemconres.2013.10.007.
642 [47] H. Manzano, J.S. Dolado, A. Ayuela, Elastic properties of the main species present in
643 Portland cement pastes, Acta Mater. 57 (2009) 1666–1674.
644 doi:10.1016/j.actamat.2008.12.007.
645 [48] J.W. Bullard, P.E. Stutzman, Analysis of CCRL Portland Cement Proficiency Samples
646 Number 151 and Number 152 Using the Virtual Cement and Concrete Reference
647 Laboratory, Cem. Concr. Res. 36 (2006) 1548–1555.
648 [49] S. Haussühl, Elastische und thermoelastische Konstanten von K2SO4, Rb2SO4,
649 Cs2SO4, (NH4)2SO4, Tl2SO4 und K2Mg2(SO4)3, Acta Crystallogr. 18 (1965) 839–
650 842. doi:10.1107/S0365110X65002062.
651 [50] S. Haussühl, Elastische und thermoelastische Eigenschaften von CaSO4 · 2H2O,
652 Zeitschrift Für Krist. 122 (1965) 311–314. doi:10.1524/zkri.1965.122.3-4.311.
653 [51] W.M. Schwerdtner, J.C.-M. Tou, P.B. Hertz, Elastic properties of single crystals of
654 anhydrite, Can. J. Earth Sci. 2 (1965) 673–683. doi:10.1139/e65-047.
655 [52] P.J.M. Monteiro, C.T. Chang, The elastic moduli of calcium hydroxide, Cem. Concr.
656 Res. 25 (1995) 1605–1609. doi:10.1016/0008-8846(95)00154-9.
657 [53] J. Němeček, V. Králík, V. Šmilauer, L. Polívka, A. Jäger, Tensile strength of hydrated
658 cement paste phases assessed by micro-bending tests and nanoindentation, Cem. Concr.
659 Compos. 73 (2016) 164–173. doi:10.1016/j.cemconcomp.2016.07.010.

660 [54] T. Howind, J.J. Hughes, W. Zhu, F. Puertas, S. Goñi, M.S. Hernández, A. Guerrero, M.
661 Palacios, J.S. Dolado, Mapping of mechanical properties of cement paste
662 microstructures, Proc. 13th Int. Congr. Chem. Cem. (2011) 1–7.
663 http://oa.upm.es/12563/1/INVE_MEM_2011_106302.pdf%5Cnhttp://oa.upm.es/12563/.
664 [55] G. Constantinides, F.J. Ulm, The nanogranular nature of C-S-H, J. Mech. Phys. Solids.
665 55 (2007) 64–90. doi:10.1016/j.jmps.2006.06.003.
666 [56] C.-C. Chen, C.-C. Lin, L.-G. Liu, S. V. Sinogeikin, J.D. Bass, Elasticity of single-
667 crystal calcite and rhodochrosite by Brillouin spectroscopy, Am. Mineral. 86 (2001)
668 1525–1529. doi:10.2138/am-2001-11-1222.
669 [57] T.J. Ahrens, Mineral Physics and Crystallography: A Handbook of Physical Constants,
670 in: American Geophysical Union, Washington, D. C., 1995. doi:10.1029/RF002.
671 [58] J. Moon, S. Yoon, R.M. Wentzcovitch, P.J.M. Monteiro, First-principles elasticity of
672 monocarboaluminate hydrates, Am. Mineral. 99 (2014) 1360–1368.
673 doi:10.2138/am.2014.4597.
674 [59] P.M. Grindrod, M.J. Heap, A.D. Fortes, P.G. Meredith, I.G. Wood, F. Trippetta, P.R.
675 Sammonds, Experimental investigation of the mechanical properties of synthetic
676 magnesium sulfate hydrates: Implications for the strength of hydrated deposits on Mars,
677 J. Geophys. Res. 115 (2010) E06012. doi:10.1029/2009JE003552.
678 [60] L. Liu, A. Jaramillo-Botero, W.A. Goddard, H. Sun, Development of a ReaxFF
679 Reactive Force Field for Ettringite and Study of its Mechanical Failure Modes from
680 Reactive Dynamics Simulations, J. Phys. Chem. A. 116 (2012) 3918–3925.
681 doi:10.1021/jp210135j.
682 [61] H. Zhang, Y. Xu, Y. Gan, Z. Chang, E. Schlangen, B. Šavija, Microstructure informed
683 micromechanical modelling of hydrated cement paste: Techniques and challenges,
684 Constr. Build. Mater. 251 (2020) 118983. doi:10.1016/j.conbuildmat.2020.118983.
685 [62] P. Zhang, S.X. Li, Z.F. Zhang, General relationship between strength and hardness,
686 Mater. Sci. Eng. A. 529 (2011) 62–73. doi:10.1016/J.MSEA.2011.08.061.
687 [63] RILEM TC, Determination of the Fracture Energy of Mortar and Concrete by Means of
688 Three-Point Bend Tests on Notched Beams, 1985.
689 http://ci.nii.ac.jp/naid/10002953477/en/ (accessed January 9, 2018).
690 [64] J. Planas, M. Elices, G. V Guinea, Measurement of the fracture energy using three-point
691 bend tests: Part 2---Influence of bulk energy dissipation, Mater. Struct. 25 (1992) 305–
692 312. doi:10.1007/BF02472671.
693 [65] K. Levenberg, A method for the solution of certain non-linear problems in least squares,

694 Q Appl Math. 2 (1994) 164–168.
695 [66] V. Šmilauer, CemBase - Cement Database for Nanocem, (2016).
696 http://mech.fsv.cvut.cz/~smilauer/index.php?id=cembase (accessed August 1, 2020).
697 [67] T. Matschei, B. Lothenbach, F.P. Glasser, The role of calcium carbonate in cement
698 hydration, Cem. Concr. Res. 37 (2007) 551–558.
699 doi:10.1016/J.CEMCONRES.2006.10.013.
700 [68] L.J. Struble, P.E. Stutzman, E.R. Fuller, Microstructural Aspects of the Fracture of
701 Hardened Cement Paste, J. Am. Ceram. Soc. 72 (1989) 2295–2299. doi:10.1111/j.1151-
702 2916.1989.tb06078.x.
703 [69] Yu Zhu & Shilang Xu, Fracture properties of cement paste and mortar: an experimental
704 investigation, in: FraMCos-6, 2007.
705 [70] A. Rhardane, S. Yasir Alam, F. Grondin, Microscopically informed upscale approach of
706 modelling damage in mortar by considering matrix-to-grain interface and grain micro-
707 fracture characteristics, Theor. Appl. Fract. Mech. (2020) 102725.
708 doi:10.1016/j.tafmec.2020.102725.
709

# Micro-mechanical model

## Hydration simulation

The gradual hydration of the cement paste is processed via a hydration model, giving a representative virtual microstructure of the real cement paste.

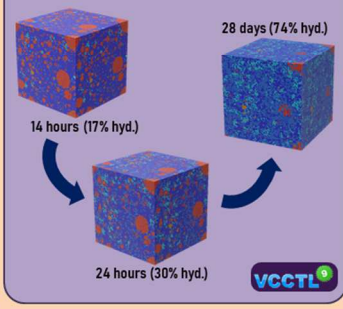


## Finite-element modelling

The intrinsic behaviour of the phases in the cement paste is reproduced using a damage model with phase properties that are known. Different boundary conditions can be imposed

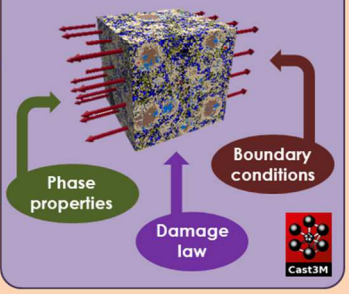


## What the model needs:

- Mineral composition of cement.
- Particle size distribution of cement.
- Water-to-binder ratio.
- Activation energy of cement.
- Temperature.
- Mass fractions of mineral additives, if any.
- No tedious experiment is needed.

Cement paste with unknown properties

## What the model provides:

| $E$ | $v$ | $f_t$ | $G_f$ |
|---|---|---|---|
| 15GPa | 0,24 | 6MPa | 8J/m² |

Mechanical properties of cement paste (needed for upscale modelling of concrete)

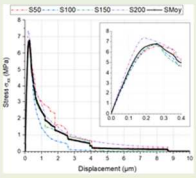


Mechanical behaviour

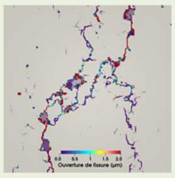

Cracking patterns

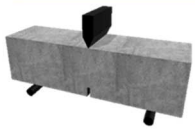

Mechanical behaviour determined!